PNAS title page

Classification: Biological Sciences, Cell Biology
Title: Self-Organization of Actin Filament Orientation in the Dendritic-Nucleation / Array-Treadmilling Model
Authors: Thomas E. Schaus[1], Edwin W. Taylor[1], and Gary G. Borisy[1,2]
[1] Department of Cell and Molecular Biology, Northwestern University Feinberg School of Medicine, 303 East Chicago Avenue, Chicago, IL 60611; [2] Marine Biological Laboratory, 7 MBL Street, Woods Hole, MA 02543
Corresponding Author: E.W. Taylor; (p) 312.503.2675; e-taylor3@northwestern.edu
Manuscript: text, 5 figs., and 2 tables; model detail and 2 videos online
Character Count: 46990 total char. equivalents
Abbreviations Footnote:

IC, SS	initial conditions, steady state
PM, LE	plasma membrane, leading edge
EM	electron micrograph
RF, FF	rigid and flexible (beam-bending) filament model
fil	filament

(No Data Deposition)

The dendritic-nucleation/array-treadmilling model provides a conceptual framework for the generation of the actin network driving motile cells. We have incorporated it into a 2-D, stochastic computer model to study lamellipodia via the self-organization of filament orientation patterns. Essential dendritic-nucleation sub-models were incorporated, including discretized actin monomer diffusion, Monte-Carlo filament kinetics, and flexible filament and plasma membrane mechanics. Model parameters were estimated from the literature and simulation, providing values for the extent of the leading edge branching/capping-protective zone (5.4 nm) and the auto-catalytic branch rate (0.43 /s). For a given set of parameters the system evolved to a steady state filament count and velocity, at which total branching and capping rates were equal only for specific orientations; net capping eliminated others. The standard parameter set evoked a sharp preference for the ±35 deg. filaments seen in lamellipodial electron micrographs, requiring ~ 12 generations of successive branching to adapt to a 15 deg. change in protrusion direction. This pattern was robust with respect to membrane surface and bending energies and to actin concentrations, but required protection from capping at the leading edge and branching angles greater than 60 deg. A +70/0/-70 deg. pattern was formed with flexible filaments ~ 100 nm or longer and with velocities less than ~ 20% of free polymerization rates.

The polymerization of soluble actin monomers between filament "barbed ends" and the plasma membrane (PM) generates the force of protrusion in cell motility (1, 2). Other proteins required for lamellipodial motility (3) are: arp2/3, which nucleates (branches) free barbed ends at ~ 70 deg. from existing ones (4); a PM-bound activator of arp2/3 (5); ADF/cofilin, which promotes the depolymerization of pointed ends (6) and perhaps debranching reactions (7); and capping protein, a terminator of barbed end growth (8). The generation and persistence of lamellipodia from these elements is described in the "dendritic-nucleation/array-treadmilling" conceptual model (2, 4, 9). This model can be sub-divided into three main processes: the kinetics of filament (de)polymerization, branching, and capping; filament-PM interactions, which limit polymerization rates; and the diffusion of actin monomers and other soluble components. Such a system is "complex" in the sense that many copies of each component type interact to exhibit "emergent" system properties not expected from the individual rules of interaction (10). In contrast to "complicated" systems of many dissimilar components with precisely defined interactions, complex systems can self-organize and adapt to environmental change.

An important emergent property is the self-organization of lamellipodial actin filaments into orientations at ±35 deg. with respect to the direction of protrusion (11, 12). Maly and Borisy predicted ±35 or +70/0/-70 deg. patterns with a 2D mathematical model based on these dendritic-nucleation assumptions (11). A model by Atilgan et al. allowed 3D branching, but required preferential arp2/3 orientation in the PM for pattern formation (13). The numerical model described here extends the Maly and Borisy model, removing most of its simplifications and limitations. Reactions are treated stochastically, the elastic properties of the membrane and filaments are included, and the time dependence of the distribution's evolution is obtained. We preserve the assumption that filaments remain oriented in the 2D lamellipodial plane. Our simulation exhibits orientational self-organization and permits the determination of a range of parameter values consistent with pattern stability. We reveal the transient development of the orientation pattern and the approach to steady state protrusion velocity and filament number.

Several computer models of (rigid) bacterial propulsion by rigid filaments have been proposed (14-16), with those of Carlsson demonstrating a flat force-velocity relationship under auto-catalytic branching (15, 16). Mogilner and Oster developed the basic theory of the actin-based elastic Brownian ratchet, which applies small-angle elastic beam theory to thermal filament fluctuations (17, 18). The present model combines stochastic propulsion and elastic filament models, adding a flexible PM load and thermodynamically realistic filament-membrane interactions.

Assumptions and Methods

A ~ 1 μm wide (X) portion of a flexible lamellipodial leading edge (LE) was simulated, with cyclic boundary conditions for all components on the ~ 1 μm Y-axis edges and a fixed actin monomer concentration $[A]_{TE}$ on the trailing edge. Every filament over the entire lamellipodial thickness was modeled, with 2D positions, orientations, and end states of each filament recorded individually. Over each small time step Δt, the calculation algorithm performed spatially-discretized (Fick's Law) diffusion and Monte-Carlo (stochastic) kinetics calculations for all components, with iterative calculations of PM and filament mechanics as required (Fig. 1, Tables 1 and 2). Consistent with experimental indication that branching and anti-capping mechanisms operate very near the LE, free barbed ends within a Y-distance ε branched new filaments at rate R_{br} and were blocked from the usual capping rate R_{cp}. New filaments deviated from the parent filament barbed end orientation by a normal distribution about the mean branch angle $\pm(\theta_{br}\pm\sigma_{br})$. Polymerization occurred at a rate proportional to the local actin monomer concentration, reduced at the LE by a Boltzmann factor based on the total system energy required for that specific protrusive step. Filaments themselves were assumed either rigid or flexible-and-cantilevered from the nearest branch or pointed end. Values for the filament and PM mechanical properties and most of the reaction rate constants were available. The main unknowns were the effective rates of branching and capping, critical to the development of the filament distribution. With R_{cp} available, ε and R_{br} were determined from simulation as illustrated in Fig. 3, completing the standard set of parameters listed in Table 2. Model details and a simulation video depicting individual protrusive steps can be found in the online *Supporting Information*.

Results and Discussion

Self-organization of filament orientation arose under any initial conditions. We first asked under what initial conditions (IC's) the model system would organize filament orientation. A set of filaments at random position, orientation, and length has no order, with only the position of the branch-inducing and capping-protective LE to generate directionality. A simulation was run under these IC's (Fig. 2a) with the branch angle standard deviation (σ_{br}) equal to zero and otherwise standard parameter conditions (Table 2). Results show the disappearance over 120 s of total filament length (mass) in most orientations, with one pair of very sharp orientations at ±35 deg. dominating (Fig. 2b and *Supporting Information* video). Because the branch angle did not vary, filament populations always occurred in strictly complementary families (related by exactly 70 deg.) and were not able to drift into other orientation families over successive generations of branching. This shows that from IC's without order, very narrow populations of filaments oriented at 35 deg. show net growth while others show net depolymerization.

When, instead of the total filament length in each direction, the *number* of filaments in each direction is plotted, we see a similar pattern with the addition of backward-facing filaments at ±105 deg. (Fig. 2c). Other orientations showed a net decrease in the number of filaments,

showing that the total capping rate outpaced the total generation rate for those orientations until their numbers reached zero. Domination by length at ±35 deg. thus did not represent a system in which ±35 deg. filaments became particularly long, but instead one in which other filament families were not viable. Filaments which faced backwards at ±105 deg. were generated at nearly the same rate as forward-facing filaments, but rapid capping away from the LE kept their total lengths (and non-productive monomer depletion) very low (Fig. 2b), and subsequent debranching and depolymerization reduced their count moderately (Fig. 2c).

It remained to be shown that the model could adapt from initial orientation patterns devoid of 35 deg. filaments into the steady state (SS) ±35 deg. patterns. This is necessary because a feature of motile cells is their ability to reorganize filament orientations in response to changes in the direction of protrusion, without which we would not observe the ±35 deg. pattern in cells which turn. Initial conditions of filaments oriented near _70/0 deg. simulated a sudden, 35 deg. clockwise turn in protrusive direction from a previous SS pattern (Fig. 2d). The standard σ_{br} of 7 deg. was used allowing the population to drift into new orientations, but no 35 deg. filaments existed initially. Orientations became symmetrical within 1 min., with a broader distribution of orientations about ±35 deg. (Fig. 2e). The SS distribution compared favorably to those measured via digital image processing techniques (Radon transform) from lamellipodial EM's (electron micrographs) (11) (Fig. 2e, with an image at SS shown in Fig. 2f). We conclude that IC's of all protrusive simulations with standard parameter values evolve and adapt into ±35 deg. patterns consistent with EM's.

Simulation indicated plausible branching parameters. The standard parameter set used in Fig. 2 and the rest of this study came from both the literature and simulation. While experimental data provided relatively direct estimates for N_{fb}, R_{cp}, and $[A]$ values, R_{br} and ε were more difficult to estimate. Modeling allowed us to determine R_{br}, ε, and the filament bending length parameter f_{ts}, consistent both with estimates for N_{fb}, R_{cp}, and $[A]$ and with experimentally accessible values such as orientation pattern and filament length.

A particular N_{fb} is set only indirectly, through filament turnover parameters R_{br}, R_{cp}, and ε. For a given V_{PM}/V_{free} the profile of N_{fb} with distance from the LE is similar (Fig. 3a, the exact shape of which will be considered in a subsequent publication). At SS, a fraction of these free barbed ends, f_ε, are within the ε-demarcated region, and the total rates of filament branching and capping are balanced: $(N_{fb}\, f_\varepsilon)\, R_{br} = (N_{fb}\, [1\_f_\varepsilon])\, R_{cp}$. The SS f_ε therefore equals $R_{cp}/(R_{br}+R_{cp})$, the setpoint for a negative feedback loop controlling N_{fb} and V_{PM}/V_{free}: A low V_{PM} relative to V_{free} allows filaments to keep up with the LE more often, raising f_ε above the setpoint. The resulting net branching increases V_{PM}/V_{free}. Conversely, a high V_{PM}/V_{free} results in net capping and a decrease in N_{fb} and V_{PM}/V_{free}.

Plots were made of the R_{br} values required to sustain a steady N_{fb} at a given ε, with two values each of N_{fb}, R_{cp}, f_{ts}, and $[A]$ specified and the diffusion coefficient (D) set very high to maintain $[A]$ uniformly (Fig. 3b). The value of $[A]$ was not a factor in the required R_{br}; it affected both V_{PM} and V_{free} ($= k_{on,brb}\,[A]\,\delta$) equally and curves are superimposed. (Comparison is therefore by V_{PM}/V_{free} throughout this study.) In contrast, maintaining higher N_{fb} values required a higher R_{br}, since the associated increase in V_{PM}/V_{free} diminished f_ε. A decrease in R_{cp} was associated with an approximately proportional decrease in required R_{br}, as expected. Filament flexibility was allowed in three parameter sets, and moderately raised the required R_{br}. The most sensitive parameter was ε itself. Decreasing ε dramatically decreased f_ε, requiring a compensatory increase in R_{br}.

In order to narrow the range of acceptable values of ε and R_{br}, the quality of the SS orientation distribution was assessed. Quality was quantified as the mean absolute deviation (α_d) from the mean orientation angle. The α_d values for all parameter sets were very similar at the same ε (and R_{br}) values, with some increase in α_d with filament flexibility (Fig 3c). Polar histograms of orientation distributions over a range of α_d showed focused distributions at high ε and noisy and distorted distributions – incompatible with EM data – at very low ε (Fig. 3d). These results are compatible with ε values as low as 1 monomer length (δ = 2.7 nm), but not less.

To limit the upper values of ε, we analyzed average filament lengths and orientation pattern development times. Again, because large ε values were associated with low R_{br}, filaments turned over slowly and thus grew very long before being capped. Using EM's, conservative visual estimates of average filament length within 1 μm of the LE range from 50 to 500 nm (not shown). In simulations, the number of filaments was a decaying function of length, with all parameter sets consistent with a maximum 500 nm average length when ε was held below 2.5 δ (Fig. 3e). Supporting this limit were measurements of the half-time of orientation pattern development ($t_{1/2}$) from a 15 deg. simulated turn (i.e. IC's of a distribution about +20 and _50 deg.), with full recovery defined as a SS α_d value. At ε = 3.0 δ, all parameter sets yielded a $t_{1/2}$ of 60 s or more (Fig. 3f), corresponding to ~ 3 min. recovery times for a minor 15 deg. turn. In comparison, fibroblasts have lamellipodial protrusion persistence times on the order of 1-2 min. before retraction (28). Length and recovery time considerations thus limited by two criteria to ε < 2.5 δ.

Of related importance to $t_{1/2}$ is the number of branching generations required for network self-organization. The product of $t_{1/2}$ and R_{br} yields the number of generations required for a 50% recovery in α_d after a rapid, 15 deg. turn (Fig. 3g). Regardless of parameter conditions, this $N_{1/2}$ value was consistently ~ 5 generations for ε = 2.0 δ. Three half-times (87.5% recovery) required 15 generations. For ε = 3.0 δ, three half times still required ~ 9 generations. These generations must be largely successive (i.e. parents branching children, then children branching grandchildren) in order for adaptation to occur.

Based on these studies, we chose a standard set of parameter values consisting of: ε = 2.0 δ; R_{cp} = 6.0 /s; and [A] = 12 μM, with which reasonable protrusion rates of 8 μm/min were achieved. Furthermore, an N_{fb} of 200 fil/μm was compatible with measurements of filament barbed end count (20) and length, and required an R_{br} of 0.43 /s. Filaments were held rigid (f_{ts} = 0) for simplicity except where noted.

The SS orientation pattern is sensitive to several model parameters. In the standard model, the same ε value limited capping protection and branching initiation. When branching was allowed at any free barbed end, regardless of position, but capping protection maintained within ε, orientation distributions remained unchanged (Fig. 4a). These conditions were effectively similar to standard conditions, since the high intrinsic capping rate quickly removed free barbed ends arising beyond ε. (While we did not simulate branching from the sides of filaments away from their barbed ends, we predict a similar result.) In contrast, when branching was only allowed within ε and capping was allowed anywhere, the orientation pattern changed dramatically. Cases in which N_{fb} and R_{br} were maintained at standard values required a greatly diminished R_{cp} of 0.22 /s, while those with standard N_{fb} and R_{cp} required a greatly elevated R_{br} of 12 /s. Both cases resulted in distributions with most filament mass facing backward,

incompatible with EM results. Protection from capping near the LE is thus essential for the formation of the ±35 deg. distribution.

Membrane model parameters were not found to significantly affect orientation distributions over a wide range of values. Given a constant R_{br}, runs varying the resistance to protrusion (γ_{se}) retained the same V_{PM} and ±35 deg. distribution due to the compensating effect of N_{fb} (Figs. 3a and 4b). This flat force-V_{PM} relationship is a characteristic of unrestrained auto-catalytic branching, observed by Carlsson (16). Membrane flexibility, specified by the bending energy coefficient, κ_b, had a significant effect on the LE shape over length scales of < 200 nm. Though the pattern is formed with respect to the LE perpendicular, this had no effect on the orientation distribution, with the same pattern attained over two orders of magnitude of κ_b variation (Fig. 4c). We attribute this stability to the LE's horizontal average orientation and rapid fluctuations relative to filament lifetime.

Conversely, filament bending stiffness had a large influence on the orientation pattern. This stiffness is dependent on the third power of effective filament bending length ($[f_{ts}\ l_{ts}]^3$, with the fraction f_{ts} simulating cross-linking). Standard parameter simulations with effective filament lengths averaging 0 (f_{ts} = 0, equivalent to rigid) or 41 nm (f_{ts} = 0.25) yielded ±35 deg. distributions, but 99 or 139 nm lengths (f_{ts} = 0.50 or 0.75, respectively) resulted in distributions similar to +70/0/_70 deg. triplets (Fig. 4d). These length limits are consistent with Mogilner and Oster's force generation calculations (17). Triplets were a result of barbed-end "splaying" to higher angles under load.

The branch angle itself (θ_{br}) was not important to the final $\pm\theta_{br}/2$ distribution over 70-110 deg., but smaller θ_{br} values resulted in a single uniform mass spanning θ_{br} (Fig. 4e). Allowing splaying by filament flexibility did not revive the two-peak distribution (not shown). Note that filaments branching from $\theta_{br}/2$ no longer face backward at θ_{br} = 60 deg., but rather 30+60 = 90 deg. This allows them an increased opportunity to further branch and disperse the population orientation. Among θ_{br} values that form two-peak distributions, the $t_{1/2}$ from IC's (uniformly distributed over the range ±90 deg.) is also sharply minimized at θ_{br} = 70 to 80 deg. (not shown). A 70 deg. branch angle is therefore optimized for rapid generation of a stable two peak orientation pattern.

Changes in V_{free} had no effect on the orientation pattern (not shown), but the ratio V_{PM}/V_{free} is important. Holding V_{free} constant, the SS V_{PM} was diminished by decreasing R_{br} (this raises the SS f_ε requirement, see Fig 3a). An R_{br} of 0.06 /s yielded V_{PM}/V_{free} = 0.20 and a ±35 deg. distribution (Fig. 4f). Decreasing R_{br} to 0.03 /s lowered the SS V_{PM}/V_{free} to 0.16 and produced a SS triplet distribution, but also lowered N_{fb} to 80 fil/μm. Raising γ_{se} to restore N_{fb} had no effect on the distribution or V_{PM}/V_{free} (plotted). Note that low R_{br} can lead to long filament lengths and slow self-organization (Fig. 3), and triplet patterns *in vivo* would be more suggestive of a small ε value (which instead lowers V_{PM} to reach the same required f_ε). Note also that, on average, a 70 deg. filament advances at V_{free} cos (70) = 0.34 V_{free}, but that stochastically-growing filaments bounded ahead by the PM do not maintain a high f_ε at this velocity and in fact require V_{PM}/V_{free} < 0.20 to dominate under standard values.

The evolution of the final orientation pattern and the development of the SS V_{PM} were interdependent. From IC's of a small number of filaments at random orientation, Fig. 5a tracks the total number of filaments in each of three complementary-orientation "families" over time. At the low N_{fb} and V_{PM} values early in the simulation, the +70/0/_70 deg. triplet multiplied at the

highest rate. With increasing V_{PM}, however, the number of filaments decreased in turn for each family until only the ±35 deg. pair remained at SS V_{PM}.

Following Maly and Borisy's evolutionary "fitness" concept, *fitness* = (rate of change of N_{fb})/(N_{fb}) for each orientation. The value is positive if a population is growing in number, zero if constant, and negative if decreasing toward extinction. Figure 5b shows the *fitness* landscape for standard branching parameters as a function of ϕ_{fil} and V_{PM}/V_{free}, with the two symmetric patterns, +70/0/_70 and ±35 deg., having maximum fitness at low and high velocities, respectively. When either pattern is rotated slightly, the capping rate of the filament with the largest ϕ_{fil} increases faster than the branching rate of its parent, causing a net decrease in fitness. Because ~ 2/3 of new filaments branching from the triplet contribute to the pattern (1/2 each of branches from ±70 deg filaments, and 2/2 branches from 0 deg. filaments ~ 4 of 6 new filaments), while only 1/2 of branches from ±35 deg. filaments contribute to their pattern, the triplet has a superior reproductive rate and fitness at low velocities. At higher protrusion rates, this effect is overcome by the low f_ε of slow 70 deg. filaments.

In order to identify the SS condition from Fig. 5b, we note that, under any model context, an increase in SS N_{fb} always increases SS V_{PM}/V_{free} due to the higher net rate of protrusive kinetic events (Fig 5c). A typical path through the fitness landscape can therefore be shown as a Darwinian evolution of patterns through the flattened landscape representation in Fig. 5d. At low N_{fb}, all forward-facing orientations interact with the same low-velocity PM and exhibit net branching ($f_\varepsilon R_{br} > [1\_f_\varepsilon] R_{cp}$ for every ϕ_{fil}). This leads to an increase in N_{fb} and V_{PM} and to an environment in which filaments at orientations near 0 and ±70 deg. decrease in count (i). Because any V_{PM} with orientations of positive fitness will ultimately result in an increased total N_{fb}, this cycle will continue (ii) until reaching the equilibrium V_{PM} and its only viable orientations, near ±35 deg. There, $f_\varepsilon R_{br} = [1\_f_\varepsilon] R_{cp}$ for 35 deg. filaments (i.e. fitness = 0) but all other orientations are driven to extinction by net capping. Given different branching parameter values consistent with a low V_{PM}, the triplet reproduces itself at a higher rate than the two-peak distribution, consequently mandating a slightly higher equilibrium V_{PM} and the extinction of the ±35 deg. pattern. In either case, populations of orientations reproduce and drive environmental changes (V_{PM}/V_{free}) which lead to changes in fitness and, ultimately, to a single symmetric pattern and velocity.

Conclusions

We have developed a comprehensive 2D model of lamellipodial protrusion based on the dendritic-nucleation/array-treadmilling mechanism, incorporating diffusion, stochastic kinetics, and elastic filament and PM models. A "standard" set of model parameter values were determined both directly from the literature and indirectly, using the criteria that model results of filament length, orientation patterns, and development times must be consistent with observed properties. Following these criteria, free barbed ends were protected from capping and allowed to branch at R_{br} = 0.43 /s within a distance ε of 5.4 nm from the leading edge. This conferred the only directionality to the system.

The model accounts for the essential dynamic properties of the network, including a negative feedback loop, controlling the fraction of free barbed ends within ε, that maintained a constant SS protrusion rate V_{PM} regardless of load. Under standard parameter values, the system converged from any IC's. to a SS V_{PM}/V_{free} of 0.38 and a free barbed end count N_{fb} of 200 /μm. The filament orientation pattern also self-organized, with only a ±35 deg. pattern remaining at this "terminal" V_{PM}. The system in fact displayed the hallmark adaptation to this pattern from

distributions initially devoid of ±35 deg. filaments. Any deviation from the symmetrical orientation increased the capping rate at the larger angle more than it increased the branching rate at the smaller angle. Changes in the direction of protrusion were thus corrected for by preferential reproduction of newly-symmetrical patterns generated via branching angle "errors."

Alternate parameter values which resulted in a SS $V_{PM}/V_{free} < 0.20$ (e.g. very low R_{br}) resulted in a _70/0/70 deg. pattern. Altering V_{free} alone had no effect. Protection from capping within ε was absolutely required for realistic pattern formation, although branching localization was not. The pattern was robust with respect to PM surface and bending energies, but sensitive to filament bending lengths longer than ~ 50 nm. These robustness and sensitivity traits describe a self-organizing filament network that resists environmental pressures in maintaining a characteristic orientation pattern and protrusion velocity.

We thank the reviewers for valuable comments. This work was supported by the National Institutes of Health (GM 62431 to GGB) and the Northwestern University Pulmonary and Critical Care Division (T32 to TES).

1. Miyata, H. & Hotani, H. (1992) *Proc Natl Acad Sci U S A* **89,** 11547-11551.
2. Pollard, T. D. & Borisy, G. G. (2003) *Cell* **112,** 453-465.
3. Loisel, T. P., Boujemaa, R., Pantaloni, D., & Carlier, M. F. (1999) *Nature* **401,** 613-616.
4. Mullins, R. D., Heuser, J. A., & Pollard, T. D. (1998) *Proc Natl Acad Sci U S A* **95,** 6181-6186.
5. Stradal, T. E. & Scita, G. (2006) *Curr Opin Cell Biol* **18,** 4-10.
6. Carlier, M. F., Laurent, V., Santolini, J., Melki, R., Didry, D., Xia, G. X., Hong, Y., Chua, N. H., & Pantaloni, D. (1997) *J Cell Biol* **136,** 1307-1322.
7. Blanchoin, L. & Pollard, T. D. (1999) *J Biol Chem* **274,** 15538-15546.
8. Wear, M. A., Yamashita, A., Kim, K., Maeda, Y., & Cooper, J. A. (2003) *Curr Biol* **13,** 1531-1537.
9. Blanchoin, L., Amann, K. J., Higgs, H. N., Marchand, J. B., Kaiser, D. A., & Pollard, T. D. (2000) *Nature* **404,** 1007-1011.
10. Ottino, J. M. (2004) *Nature* **427,** 399.
11. Maly, I. V. & Borisy, G. G. (2001) *Proc Natl Acad Sci U S A* **98,** 11324-11329.
12. Verkhovsky, A. B., Chaga, O. Y., Schaub, S., Svitkina, T. M., Meister, J. J., & Borisy, G. G. (2003) *Mol Biol Cell* **14,** 4667-4675.
13. Atilgan, E., Wirtz, D., & Sun, S. X. (2005) *Biophys J* **89,** 3589-3602.
14. Alberts, J. B. & Odell, G. M. (2004) *PLoS Biol* **2,** e412.
15. Carlsson, A. E. (2001) *Biophys J* **81,** 1907-1923.
16. Carlsson, A. E. (2003) *Biophys J* **84,** 2907-2918.
17. Mogilner, A. & Oster, G. (1996) *Biophys J* **71,** 3030-3045.
18. Mogilner, A. & Oster, G. (2003) *Biophys J* **84,** 1591-1605.
19. McGrath, J. L., Tardy, Y., Dewey, C. F., Jr., Meister, J. J., & Hartwig, J. H. (1998) *Biophys J* **75,** 2070-2078.
20. Abraham, V. C., Krishnamurthi, V., Taylor, D. L., & Lanni, F. (1999) *Biophys J* **77,** 1721-1732.
21. Boal, D. (2002) *Mechanics of the Cell* (Cambridge University Press, Cambridge).
22. Isambert, H., Venier, P., Maggs, A. C., Fattoum, A., Kassab, R., Pantaloni, D., & Carlier, M. F. (1995) *J Biol Chem* **270,** 11437-11444.

23. Pollard, T. D. (1986) *J Cell Biol* **103,** 2747-2754.
24. Pollard, T. D. & Cooper, J. A. (1984) *Biochemistry* **23,** 6631-6641.
25. Blanchoin, L., Pollard, T. D., & Mullins, R. D. (2000) *Curr Biol* **10,** 1273-1282.
26. Schafer, D. A., Jennings, P. B., & Cooper, J. A. (1996) *J Cell Biol* **135,** 169-179.
27. Mejillano, M. R., Kojima, S., Applewhite, D. A., Gertler, F. B., Svitkina, T. M., & Borisy, G. G. (2004) *Cell* **118,** 363-373.
28. Bear, J. E., Svitkina, T. M., Krause, M., Schafer, D. A., Loureiro, J. J., Strasser, G. A., Maly, I. V., Chaga, O. Y., Cooper, J. A., Borisy, G. G.*, et al.* (2002) *Cell* **109,** 509-521.

Fig. 1. Lamellipodia were simulated using three sub-models: (lower left) A fixed rectangular grid demarcated regions of uniform actin concentration, subject to Fick's diffusion relation between them. (right) Within each time step, kinetic reactions were carried out stochastically for every filament. (top) Minimization of plasma membrane and filament potential energies yielded quasi-steady-state geometries between kinetic states.

Fig. 2. Filaments in the model spontaneously self-organized from any initial conditions (IC's) into preferential orientations ±35 deg. from the leading edge perpendicular. (a) IC's of simulations in (b, c), showing random filament barbed-end position, orientation (0-360 deg.), and length (0-150 nm) over 0.5 x 0.35 μm of a 1 x 1 μm simulation. Fifty percent of filaments shown; standard parameter set of Table 2, except σ_{br} = 0 deg.; free barbed ends labeled green. (b) Polar histogram plots of total filament length versus orientation displayed a sharp preference for ±35 deg. orientations, with loss of others. (c) Plotted by number of filaments, a similar pattern was observed but with backward-facing filaments made obvious. (d) IC's of standard parameter simulations (σ_{br} = 7 deg.) in (e, f), showing orientations near _70/0 deg. (e) Polar plots of total length over time show adaptive behavior, and compare favorably with EM measurements at SS. (f) Image of a 0.5 x 0.5 μm section at SS. Capped barbed ends labeled red, blue dots denote branches. At SS, the 1 x 1 μm simulation contained 700 filaments totaling 250 μm in length, with 200 free barbed ends.

Fig. 3. Orientation pattern and filament length were examined for several parameter sets to determine standard branching parameters. (a) The distribution of Y-distances from free barbed ends to the LE is shown for standard conditions (R_{br} = 0.43 /s, f_ε = 0.93, and V_{PM}/V_{free} = 0.36, blue) and a reduced N_{fb} of 140 fil/μm (R_{br} = 0.21 /s, f_ε = 0.97, and V_{PM}/V_{free} = 0.28, red). (b) For all conditions, the R_{br} required to sustain the specified N_{fb} increased sharply at low ε. (c) The extent of filament deviation from the average orientation (α_d) increased from near σ_{br} to above 30 deg. at ε = 0.5 δ under all conditions. (d) Orientation patterns for 3 α_d values plotted, with backward-facing filaments rotated by 180 deg. to make them comparable to EM data, suggested a lower limit of $\varepsilon \sim 1.0\ \delta$. (e) High ε resulted in unreasonably long filament lengths, restricting ε to $< 2.5\ \delta$. (f) The half-time to develop a SS pattern ($t_{1/2}$) from an initial 15 deg. asymmetry also increased with ε, supporting $\varepsilon < 3\ \delta$. (g) The characteristic number of branching generations required to approach SS ($N_{1/2}$) was similar for all parameter sets at a given ε (2.0 δ shown).

Fig. 4. Sensitivity of patterns to non-branching parameters further suggested limits to *in vivo* values. Polar plots include all filaments in a LE 1 x 1 μm area. (a) Deviating from standard conditions, maintaining branching pressure but allowing capping anywhere resulted in a non-physiologic, high backward-filament mass. (b) Altering surface energy (γ_{se}) values alone did not affect orientation pattern. (c) Varying PM bending energy (κ_B) altered the variability in LE shape but did not alter the pattern. (d) Simulations with varying filament flexibility all had average terminal segment lengths (l_{ts}) of ~ 200 nm. When effective bending lengths exceeded ~ 41 nm, orientation patterns similar to +70/0/_70 deg. distributions resulted. (e) Setting the mean branching angle (θ_{br}) near or under 60 deg. resulted in a single distribution. (f) Velocities of at least ~ 20% of V_{free} were required for ±35 deg. orientation patterns.

Fig. 5. The orientations of maximum fitness vary with V_{PM}/V_{free}, but the SS pattern is that with zero fitness at the equilibrium V_{PM}. (a) The sum of +70/0/_70 deg. filaments grew fastest in number at low N_{fb} and V_{PM}, but only the ±35 deg. population remained at SS V_{PM}. (standard conditions with σ_{br} = 0 deg. and a rigid PM for clarity) (b) The 3D fitness landscape for standard conditions. (c) V_{PM}/V_{free} rises with N_{fb}. (d) A 2D representation of (b) shows positive (green) or negative (red) fitness at a given velocity and orientation. At low V_{PM}/V_{free}, all orientations undergo net reproduction, raising N_{fb} and V_{PM}/V_{free}. The "terminal" V_{PM} is achieved by – and limited to – the ±35 deg. family.

(The figures follow this page, in order)

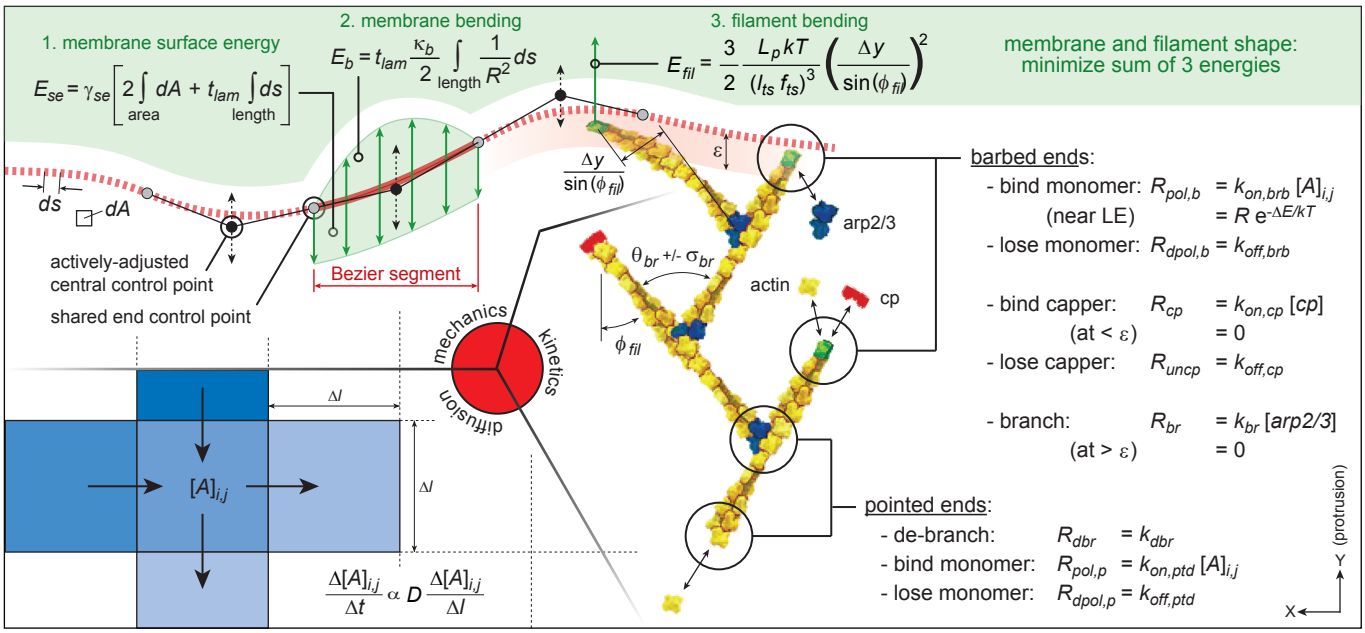
1. membrane surface energy
$E_{se} = \gamma_{se}\left[2\int_{area} dA + t_{lam}\int_{length} ds\right]$
2. membrane bending
$E_b = t_{lam}\frac{\kappa_b}{2}\int_{length}\frac{1}{R^2}ds$
3. filament bending
$E_{fil} = \frac{3}{2}\frac{L_p kT}{(l_{ts} f_{ts})^3}\left(\frac{\Delta y}{\sin(\phi_{fil})}\right)^2$
membrane and filament shape: minimize sum of 3 energies
ds
dA
actively-adjusted central control point
shared end control point
Bezier segment
$\frac{\Delta y}{\sin(\phi_{fil})}$
ε
arp2/3
actin
cp
θ_{br} +/- σ_{br}
ϕ_{fil}
mechanics
kinetics
diffusion
Δl
$[A]_{i,j}$
Δl
$\frac{\Delta[A]_{i,j}}{\Delta t} \alpha D \frac{\Delta[A]_{i,j}}{\Delta l}$
barbed ends:
- bind monomer: $R_{pol,b} = k_{on,brb}\,[A]_{i,j}$
(near LE) $= R\, e^{-\Delta E/kT}$
- lose monomer: $R_{dpol,b} = k_{off,brb}$
- bind capper: $R_{cp} = k_{on,cp}\,[cp]$
(at < ε) $= 0$
- lose capper: $R_{uncp} = k_{off,cp}$
- branch: $R_{br} = k_{br}\,[arp2/3]$
(at > ε) $= 0$
pointed ends:
- de-branch: $R_{dbr} = k_{dbr}$
- bind monomer: $R_{pol,p} = k_{on,ptd}\,[A]_{i,j}$
- lose monomer: $R_{dpol,p} = k_{off,ptd}$
Y (protrusion)
X

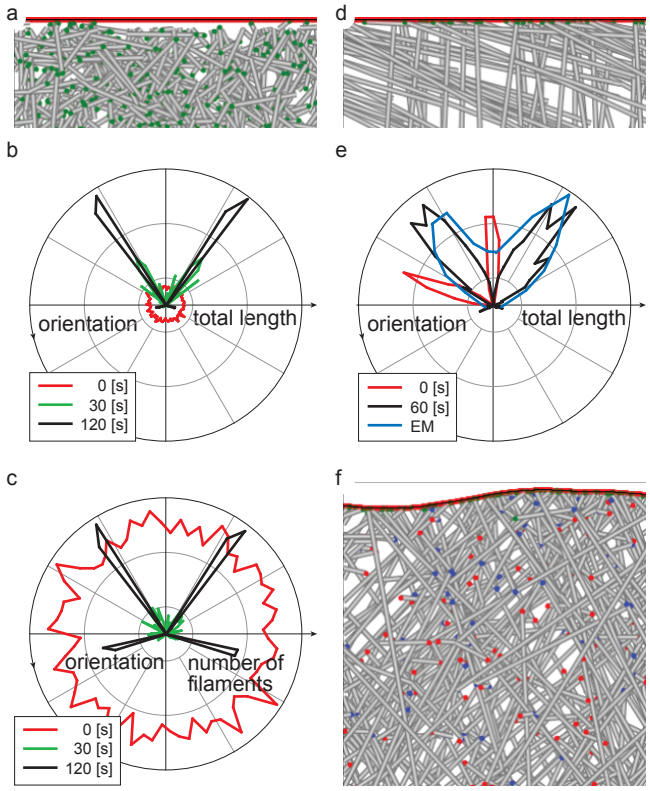
a
d
b
e
orientation
total length
0 [s]
30 [s]
120 [s]
orientation
total length
0 [s]
60 [s]
EM
c
f
orientation
number of filaments
0 [s]
30 [s]
120 [s]

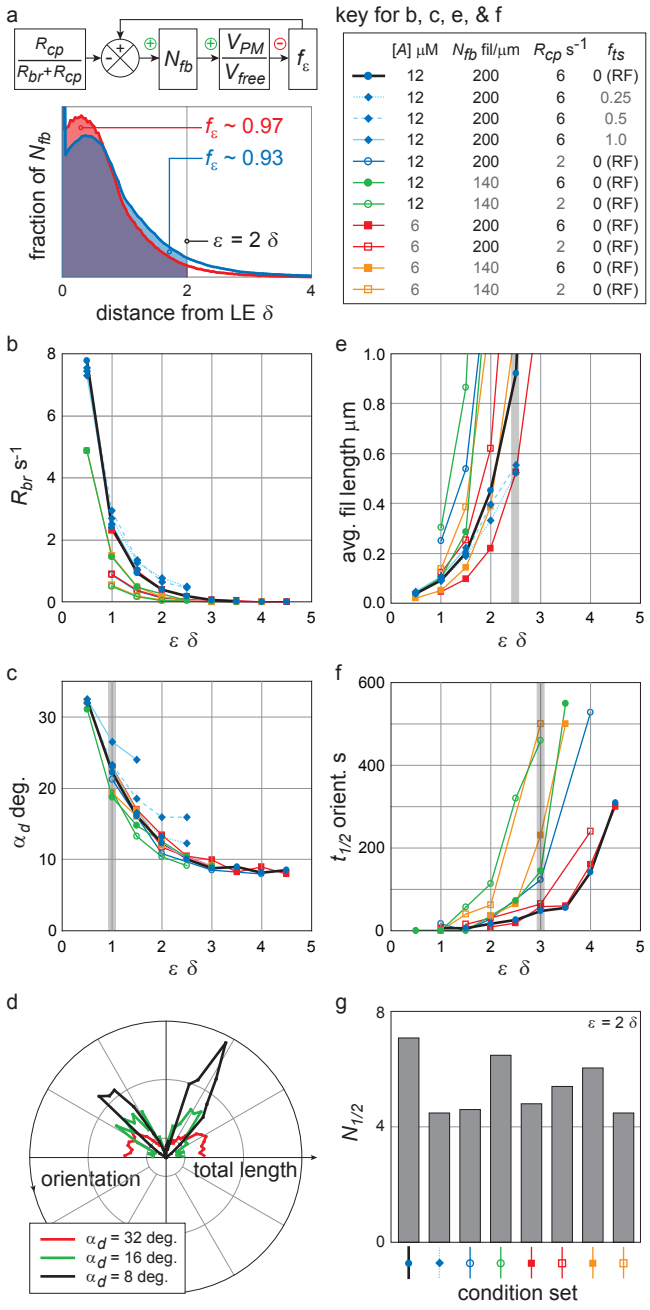
a
$\frac{R_{cp}}{R_{br}+R_{cp}}$
N_{fb}
$\frac{V_{PM}}{V_{free}}$
f_ε
fraction of N_{fb}
f_ε ~ 0.97
f_ε ~ 0.93
ε = 2 δ
distance from LE δ
key for b, c, e, & f
[A] μM
N_{fb} fil/μm
R_{cp} s^{-1}
f_{ts}
12 200 6 0 (RF)
12 200 6 0.25
12 200 6 1.0
12 200 2 0 (RF)
12 140 6 0 (RF)
12 140 2 0 (RF)
6 200 6 0 (RF)
6 200 2 0 (RF)
6 140 6 0 (RF)
6 140 2 0 (RF)
b
R_{br} s^{-1}
ε δ
e
avg. fil length μm
ε δ
c
α_d deg.
ε δ
f
$t_{1/2}$ orient. s
ε δ
d
orientation
total length
α_d = 32 deg.
α_d = 16 deg.
α_d = 8 deg.
g
ε = 2 δ
$N_{1/2}$
condition set

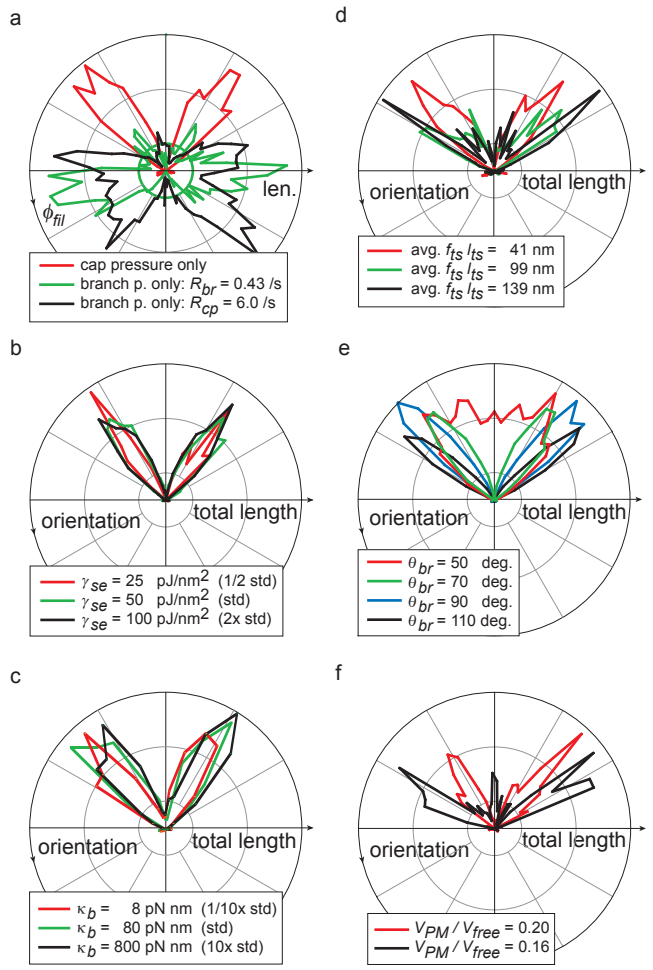
a
len.
ϕ_{fil}
cap pressure only
branch p. only: R_{br} = 0.43 /s
branch p. only: R_{cp} = 6.0 /s
d
orientation
total length
avg. f_{ts} l_{ts} = 41 nm
avg. f_{ts} l_{ts} = 99 nm
avg. f_{ts} l_{ts} = 139 nm
b
orientation
total length
γ_{se} = 25 pJ/nm^2 (1/2 std)
γ_{se} = 50 pJ/nm^2 (std)
γ_{se} = 100 pJ/nm^2 (2x std)
e
orientation
total length
θ_{br} = 50 deg.
θ_{br} = 70 deg.
θ_{br} = 90 deg.
θ_{br} = 110 deg.
c
orientation
total length
κ_b = 8 pN nm (1/10x std)
κ_b = 80 pN nm (std)
κ_b = 800 pN nm (10x std)
f
orientation
total length
V_{PM} / V_{free} = 0.20
V_{PM} / V_{free} = 0.16

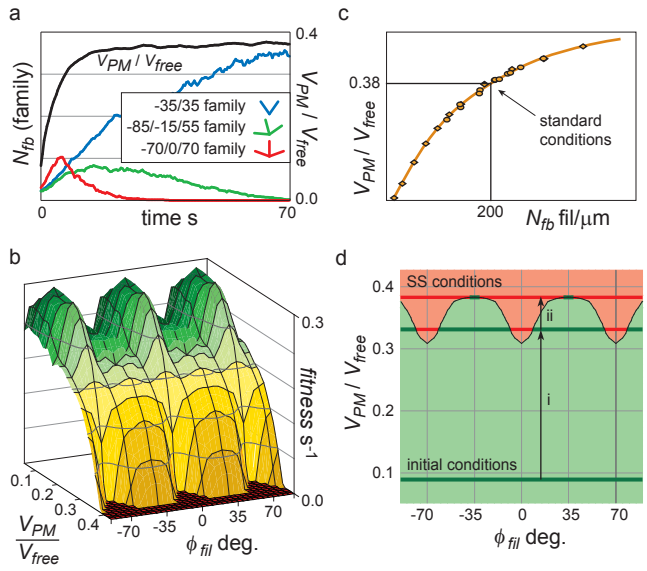
a
N_{fb} (family)
V_{PM} / V_{free}
V_{PM} / V_{free}
0.4
0.0
-35/35 family
-85/-15/55 family
-70/0/70 family
0
time s
70
b
fitness s^{-1}
0.3
0.0
0.1
0.2
0.3
0.4
$\frac{V_{PM}}{V_{free}}$
-70
-35
0
35
70
ϕ_{fil} deg.
c
0.38
V_{PM} / V_{free}
standard
conditions
200
N_{fb} fil/μm
d
SS conditions
ii
i
initial conditions
0.4
0.3
0.2
0.1
V_{PM} / V_{free}
-70
-35
0
35
70
ϕ_{fil} deg.

Table 1. Symbols

R	radius of curvature of the LE in the plane of simulation
V_{PM}; V_{free}	velocity of the LE center of mass; free polymerization velocity
ΔE	thermal energy required for intercalating a monomer between LE and barbed end = $\Delta(\Sigma E_b + \Sigma E_{se} + \Sigma E_{fil})$ over successive potential states
E_b; E_{se}; E_{fil}	PM bending, PM surface, and filament bending potential energies
ds; dA	differential length along LE; differential area of plasma membrane
l_{ts}	filament terminal segment length, from barbed end to first branch
ϕ_{fil}	filament orientation angle, with respect to the direction of protrusion
α_d	mean absolute fil. deviation angle, measured from population mean
$[A]$; $[A]_{i,j}$	ATP-G-actin concentration, in general; local conc. at position (i,j)
f_ε	avg. fraction of all free barbed ends within the ε-demarcated LE zone
$t_{1/2}$; $N_{1/2}$	half-time; no. of branching generations to develop orientation pattern

Table 2. Model parameters and standard values

symbol	value	description	ref's
δ	2.7 nm	extension length of polymerizing actin monomer	-
D	6.0 $\mu m^2/s$	cytoplasmic actin monomer diffusion coefficient	19
$[A]_{TE}$	12 μM	fixed, trailing edge actin monomer concentration	20
γ_{se}	50 pJ/nm^2	plasma membrane surface energy coefficient	18,21
κ_b	80 pN nm	bending energy coefficient, ~ 20 kT	21
L_p	10 μm	persistence length of actin filaments	22
t_{lam}	200 nm	lamellipodial thickness	20
$k_{on,brb}$	12 /μM/s	on-rate of actin to barbed end _ $R_{pol,b}/[A]$	23
$k_{off,brb}$	1.4 /s	off-rate of actin from barbed end _ $R_{dpol,b}$	23
$k_{on,ptd}$	0 /μM/s	on-rate of actin to ptd. end, profilin-adj. _ $R_{pol,p}/[A]$	24
$k_{off,ptd}$	8.0 /s	off-rate of actin from ptd. end, cofilin-adj. _ $R_{dpol,p}$	6
ε	2.0 δ	LE cap-protection/branch zone (Y) length	15
R_{br}	0.43 /s	(total) rate of barbed end branching _ k_{br} [*arp2/3*]	18,20
R_{dbr}	0.05 /s	rate of debranching for any branch point	25
R_{cp}	6.0 /s	rate of barbed end capping _ $k_{on,cp}$ [*cp*]	26
R_{uncp}	0 /s	uncapping rate for any capped barbed end _ $k_{off,cp}$	26,27
N_{fb}	200 fil/μm	free barbed ends per LE width (indirectly spec.)	20
θ_{br}	70 deg.	average branch angle	4
σ_{br}	7 deg.	branch angle standard deviation	4
Δt	0.0004 s	simulation time step	-
f_{ts}	0 (_ rigid)	fraction of terminal segment length in fil bending	text

Supporting Information

Video 1 (see PNAS site)
Small, 0.2 x 0.2 μm simulation under standard conditions (of Table 1) and 10 initial filaments. Red dots denote capped barbed ends, green dots denote free barbed ends, and blue dots denote arp2/3 branch points. Video shows the interaction of individual, polymerizing, barbed ends of rigid-filaments and a flexible plasma membrane. Note also the branching and depolymerization reactions.

Video 2 (see PNAS site)
Larger, 1 x 1 μm simulation (of Fig. 2a-c), from initial conditions of random filament length, orientation, and position. The polar histogram shows the number of filaments at each orientation. The red histogram denotes only filaments with ε of leading edge, while the black histogram accounts for all filaments in the simulation area.

Model Details
A rectangular portion of a lamellipodial leading edge (LE) was simulated, measuring up to 5 μm wide ("X" direction) by 5 μm long ("Y" direction). Cyclic boundary conditions coupled the Y-axis edges for diffusion exchange, membrane shape, and filament continuity. This eliminated potential edge effects, in essence mapping the rectangular simulation onto a cylinder. A flexible plasma membrane (PM) bounded all filaments and soluble monomers at the LE, and the trailing edge of the simulation was fixed at a free actin monomer concentration, $[A]_{TE}$, and absorptive to filaments crossing the boundary. Given the small relative thickness of the lamellipodium (~ 0.2 μm in the dorsal-ventral "Z" direction (1)), no values were resolved in the Z direction. Every filament in the entire lamellipodial thickness was modeled, with 2D positions, orientations, and end states of each filament recorded individually. Because filaments typically take only ~ 5% of the lamellipodial volume (1), steric hindrance between filaments was neglected.

The calculation algorithm was a hybrid of dissimilar sub-models, with spatially-discretized diffusion calculations, Monte-Carlo (stochastic) filament kinetics, and iterative calculations of PM and filament mechanics based on analytical energy relationships (Fig. 1). The simulations were divided into small time-steps (Δt), each of which consisted of diffusion calculations over the entire simulated area, kinetics calculations for each filament individually, and membrane and filament mechanics calculations as needed. The small Δt served to both maintain stability in diffusion calculations and to impart randomness to the order of kinetic events on different filaments.

Diffusion of actin monomers was calculated using a discretized Fick's relationship (Fig. 1). The rectangular simulation area was subdivided into a grid of smaller rectangles (~ 100 nm per side), each of which was assumed to have a single, spatially-averaged actin monomer concentration, $[A]_{i,j}$. Filament (de)polymerization reactions were immediately accompanied by appropriate concentration adjustments to the grid rectangle at which the filament end was located. Although the LE shape was allowed to change in flexible PM simulations, the grid

remained fixed with respect to the LE. All other soluble components were assumed constant spatially and temporally.

Filament kinetics were simulated using only well-established kinetic reactions. At each time step, a Monte-Carlo algorithm processed each filament in turn for the probability of branching, debranching, capping, polymerization, and depolymerization reactions at both pointed and barbed ends, as appropriate (Fig. 1, Table 1 for constants). Free barbed end tip positions within a Y-distance ε from the LE branched new filaments at a constant rate (auto-catalytic branching), but any temporary tethering between arp2/3 and the membrane-bound activator was neglected (2). New filament orientation deviated from the parent filament barbed end orientation by a normal distribution about the average branch angle ($\theta_{br} \pm \sigma_{br}$), and was equally likely to face more toward or away from the LE (i.e. no "intelligent" branching). As suggested by the existence of electron micrograph (EM) orientation patterns (3), branching was restricted to the plane of simulation. Monomer orientation within the filament and its effect on branching orientation about the axis of the parent filament was thus neglected. Debranching at a constant rate released the pointed end of the daughter filament to a free state (4).

Because productive, forward-facing barbed ends are thought to be protected from capping by the VASP protein (5), or are uncapped by PM-supplied PIP or PIP_2 (6), protection from capping was applied within the same distance ε from the LE as used for branching. We assumed capped ends remained effectively capped for the lifetime of the filament, as evidence shows either capped end lifetimes are long compared to filament lifetimes (6), or capping protein is removed rapidly but replaced by another capper (7).

Filament polymerization occurred at a rate proportional to the local G-actin concentration $[A]_{i,j}$, and F-actin nucleotide states were neglected. When filament polymerization required an increase in system potential energy (i.e. protrusion), the kinetic rate was multiplied by a Boltzmann term ($e^{-\Delta E/kT}$, where $kT = 4.13\text{E-}21$ J), accounting for the probability that the required thermal energy (ΔE) was available to create at least a monomer-size space between the filament and the PM (8). No regard was thus paid to the path taken between kinetic states. As is usually done in similar kinetics simulations (9, 10), and in the absence of data, the entire Boltzmann probability factor was applied to the kinetic on-rate, while the off-rate (of depolymerization) remained fixed. Note that this method did not require nor use any system-level force-velocity relationship; the protrusion rate, V_{PM}, resulted directly from the sum of protrusive reactions, each occurring according to fundamental energetic principles.

The probability of each (de)polymerization event was treated independently for each free barbed end at each time step. This was possible because the average time between unimpeded monomer additions ($(k_{on,brb}\,[A])^{-1} \sim 7000$ μs) is much longer than the correlation times for filament tip and local PM position under thermal motion (< 1 μs each (11)). The entire system was therefore able to come to a new quasi-equilibrium geometry between successive polymerization events, and probabilities based on energy differences could be calculated independently.

The equilibrium geometry and total potential energy of the simulated system (all filaments and the entire PM) between kinetic states were attained by vertically moving nodes controlling local PM (LE) positions (see below). Given the positions of the rigid filament bases and their bending energies, as well as PM bending and surface energies, all PM nodes were adjusted until the total system potential energy was minimized. Adjustment of the nodes altered not only PM energy, but required filament bending under the constraint that all filament tips must remain in the "cytoplasm." When considering a polymerization event, the same calculation

was then repeated with a "test" monomer added to the filament of interest, and the difference in total system energies (ΔE) was used in the Boltzmann probability term.

In the simpler of two mechanical filament models, filaments were assumed to be straight and fixed in position with respect to the substrate. This implied perfect rigidity and connection to substrate adhesions, realized by treating filaments as unyielding constraints supporting the PM. In the second model, filament bending was allowed according to a cantilever beam-bending energy relationship with small-angle approximations (Fig. 1). Here, filament barbed ends supported and protruded the LE with a stiffness inversely proportional to their bending length cubed ($[l_{ts} * f_{ts}]^3$). Bending lengths were assumed to be the length of the terminal filament segment (l_{ts}), spanning from the growing barbed end to the nearest arp2/3 branch point (or pointed end if un-branched), beyond which the filament was assumed anchored in position and orientation. This length was decreased by a constant factor ($0 < f_{ts} < 1$) to account for stiffening by cross-links to other filaments. Assignment of $f_{ts} = 0$ is equivalent to specifying rigid filaments, as done in the standard conditions of Table 1. Both models neglected myosin-mediated network distortion, not required for motility (8). We regard the model as simulating near the LE any combination of protrusive or retrograde flow, and any distinction between them a matter of coordinate system.

The shape of the LE represented an equilibrium between PM bending and surface energy forces for a given set of filament constraints (Fig. 1). The surface energy was taken as proportional to the total membrane surface area with a proportionality constant γ_{se}. It served to minimize both in-plane (X-Y) and edge (X-Z) components of PM area, consequently distorting the LE. While live cells are approximately spherical in suspension, they increase their surface area by an order of magnitude upon substrate adhesion. Because this is far more expansion than is possible from stretching inter-lipid distances before membrane tearing, and cells appear to operate similarly under a wide range of surface areas, we assumed than the cell under consideration has a mechanism of supplying extra membrane for protrusion under a constant tension. That is, we assumed that γ_{se} was insensitive to the total surface area changes encountered over cycles of LE protrusion (modeled) and trailing edge retraction (assumed). The tendency of this surface energy to bend the LE was countered by a bending energy term, inversely proportional to the square of the local radius with a stiffness constant κ_B, which acted to straighten the LE. Only in-plane flexibility was considered; the stiffness added by the dorsal-ventral curvature of the LE was neglected.

Computationally, the LE shape was modeled as a contiguous series of quadratic Bezier spline curves, with control points spaced equally in the X-direction. End-control points were shared and taken as the midpoint between central control points of adjacent curves, ensuring that all adjacent splines were continuous in both position and slope. Thirty splines per micron were typically used, allowing for a generalized shape, and no discernable change in simulation results were obtained by increasing this number. At each call, the mechanics subroutines adjusted the Y-positions of all central control points iteratively to achieve the global minimum potential energy. (See video 1 in the online *Supporting Information*, recorded in high temporal and spatial resolution.)

References

1. Abraham, V. C., Krishnamurthi, V., Taylor, D. L., & Lanni, F. (1999) *Biophys J* **77,** 1721-1732.

2. Marcy, Y., Prost, J., Carlier, M. F., & Sykes, C. (2004) *Proc Natl Acad Sci U S A* **101,** 5992-5997.
3. Maly, I. V. & Borisy, G. G. (2001) *Proc Natl Acad Sci U S A* **98,** 11324-11329.
4. Blanchoin, L., Pollard, T. D., & Mullins, R. D. (2000) *Curr Biol* **10,** 1273-1282.
5. Bear, J. E., Svitkina, T. M., Krause, M., Schafer, D. A., Loureiro, J. J., Strasser, G. A., Maly, I. V., Chaga, O. Y., Cooper, J. A., Borisy, G. G*., et al.* (2002) *Cell* **109,** 509-521.
6. Schafer, D. A., Jennings, P. B., & Cooper, J. A. (1996) *J Cell Biol* **135,** 169-179.
7. Mejillano, M. R., Kojima, S., Applewhite, D. A., Gertler, F. B., Svitkina, T. M., & Borisy, G. G. (2004) *Cell* **118,** 363-373.
8. Theriot, J. A. (2000) *Traffic* **1,** 19-28.
9. Mogilner, A. & Oster, G. (1996) *Biophys J* **71,** 3030-3045.
10. Mogilner, A. & Oster, G. (2003) *Biophys J* **84,** 1591-1605.
11. Howard, J. (2001) *Mechanics of Motor Proteins and the Cytoskeleton* (Sinauer Associates, Inc., Sunderland).